Biomaterials 283 (2022) 121416

Contents lists available at ScienceDirect

Biomaterials

journal homepage: www.elsevier.com/locate/biomaterials

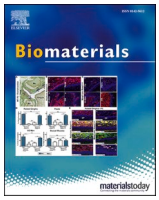

Understanding nanomedicine treatment in an aggressive spontaneous brain cancer model at the stage of early blood brain barrier disruption

Phillip W. Janowicz [a,b,c,d], Zachary H. Houston [a,b,c,e], Jens Bunt [d,h], Nicholas L. Fletcher [a,b,c,e], Craig A. Bell [a,b,c,e], Gary Cowin [a,g], Christopher B. Howard [a,b,c,f], Dewan Taslima [a,b,c], Nicholas Westra van Holthe [a,b,c], Amber Prior [a,c,e], Vanessa Soh [a,c,e], Saikat Ghosh [a,c,e], James Humphries [a,b,c], Pie Huda [a,b,c], Stephen M. Mahler [c,f], Linda J. Richards [d], Kristofer J. Thurecht [a,b,c,e,*]

[a] Centre for Advanced Imaging, The University of Queensland, Australia
[b] Australian Research Council Centre of Excellence in Convergent Bio-Nano Science and Technology, The University of Queensland, Australia
[c] Australian Institute for Bioengineering and Nanotechnology, The University of Queensland, Australia
[d] Queensland Brain Institute and School of Biomedical Sciences, The University of Queensland, Australia
[e] Australian Research Council Training Centre for Innovation in Biomedical Imaging Technology, The University of Queensland, Australia
[f] Australian Research Council Training Centre for Biopharmaceutical Innovation, The University of Queensland, Australia
[g] National Imaging Facility, The University of Queensland, St Lucia, Queensland, 4072, Australia
[h] Princess Máxima Center for Pediatric Oncology, Utrecht, Netherlands

ARTICLE INFO

Keywords:
Brain tumour
Nanomedicine
Hyperbranched polymer
Blood brain barrier
MRI
Glioblastoma
Bispecific antibody
Brain cancer

ABSTRACT

Personalised nanomedicine is an advancing field which has developed significant improvements for targeting therapeutics to aggressive cancer and with fewer side effects. The treatment of gliomas such as glioblastoma (or other brain tumours), with nanomedicine is complicated by a commonly poor accumulation of drugs in tumour tissue owing to the partially intact blood-brain barrier (BBB). Nonetheless, the BBB becomes compromised following surgical intervention, and gradually with disease progression. Increased vasculature permeability generated by a tumour, combined with decreased BBB integrity, offers a mechanism to enhance therapeutic outcomes. We monitored a spontaneous glioma tumour model in immunocompetent mice with ongoing T2-weighted and contrast-enhanced T1-weighted magnetic resonance imaging gradient echo and spin echo sequences to predict an optimal "leakiness" stage for nanomedicine injections. To ascertain the effectiveness of targeted nanomedicines in treating brain tumours, subsequent systemic administration of targeted hyperbranched polymers was then utislised, to deliver the therapeutic payload when both the tumour and brain vascularity had become sufficiently susceptible to allow drug accumulation. Treatment with either doxorubicin-loaded hyperbranched polymer, or the same nanomedicine targeted to an ephrin receptor (EphA2) using a bispecific antibody, resulted in uptake of chemotherapeutic doxorubicin in the tumour and in reduced tumour growth. Compared to vehicle and doxorubicin only, nanoparticle delivered doxorubicin resulted in increased tumour apoptosis, while averting cardiotoxicity. This suggests that polyethylene based (PEGylated)-nanoparticle delivered doxorubicin could provide a more efficient treatment in tumours with a disrupted BBB, and that treatment should commence immediately following detection of gadolinium permeability, with early detection and ongoing 'leakiness' monitoring in susceptible patients being a key factor.

1. Introduction

Brain cancer remains one of the most treatment-resistant malignancies. Glioblastoma multiforme (GBM) is the most common and aggressive primary brain malignancy with a median survival of ~15 months [1]. Current standard treatment includes maximal safe surgical

* Corresponding author. Centre for Advanced Imaging, Australian Research Council Training Centre for Innovation in Biomedical Imaging Technologies and Australian Institute for Bioengineering and Nanotechnology, Australia.
E-mail address: k.thurecht@uq.edu.au (K.J. Thurecht).

https://doi.org/10.1016/j.biomaterials.2022.121416
Received 15 November 2020; Received in revised form 13 February 2022; Accepted 15 February 2022
Available online 17 February 2022

resection of the tumour mass, followed by radiotherapy and chemotherapy with temozolomide [1]. Despite this intensive treatment, 89–96% of patients do not survive beyond 3–5 years, and there are ~227,000 deaths from brain cancer globally every year, with ~7 in 100,000 people affected by GBM in Western countries such as Australia [2,3]. One of the limitations of chemotherapeutic treatment administered intravenously is the high proportion that does not reach the brain and the subsequent side effects that eventuate due to accumulation in off-target tissues. This ultimately limits dosage and causes a loss of quality of life through damage to the peripheral organs, such as the heart, lungs, and liver [4]. It is vital for patients suffering with brain cancer that safer, more effective and efficiently targeted treatments are developed, and nanomedicine provides potential solutions towards solving this problem.

Nanomedicines are a promising strategy to target tumours with chemotherapy in a safe and controlled manner by releasing cytotoxic payloads specifically in the tumour tissue. Highly PEGylated hyperbranched polymers (HBPs) can be adopted to carry chemotherapy in a pro-drug form to the tumour site, and in recent preclinical models it has been demonstrated that this occurs with minimal side effects [5,6]. It does this by bypassing extensive immune recognition through the *in vivo* stealth properties of the PEG side-chains, and subsequently releasing the drug in the tumour environment; typically this has been achieved through cleavage of a drug linker containing an acid-cleavable hydrazone bond under conditions found in the tumour environment [7]. The enhanced permeability and retention (EPR) of HBPs in brain tumours also aids in drug delivery, whereby leaky vasculature and poor lymphatic drainage result in accumulation of nano-sized materials within the tumour. Personalised specificity and accumulation can be further enhanced by targeting these nanocarriers to common disease-specific markers, such as Ephrin A2 (EphA2) [8,9], epidermal growth factor receptor (EGFR) and others [10].

EphA2 is a receptor that is frequently overexpressed on highly proliferating brain tumour cells, making it an ideal target for

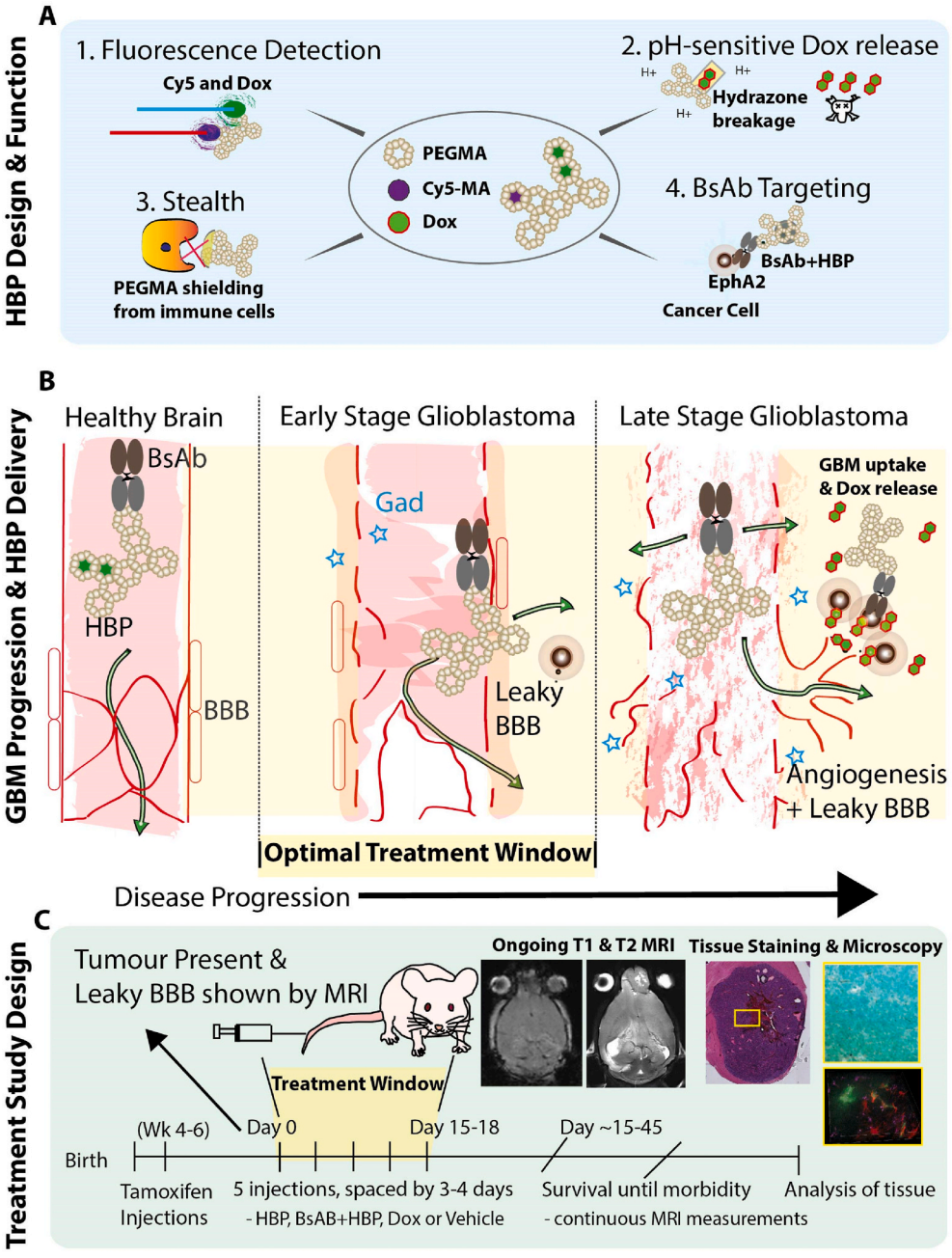

Fig. 1. Schematic of hyperbranched polymer (HBP) and treatment study design. A) The HBP has multiple functions including pH-sensitive Dox release, targeting to tumour cells, immune cell avoidance and multi-fluorescence excitability. B) The closed blood-brain barrier (BBB), which does not allow the passage of HBP, bispecific antibody (BsAb) or gadolinium (Gad) into the brain parenchyma, becomes leaky in early stage and late stage brain tumours, and angiogenesis also occurs as the disease progresses into a glioblastoma multiforme. C) Tumour bearing mice were treated with 5 injections, spaced by 3–4 days between each inejection, of either HBP-Dox, BsAb + HBP-Dox, Dox or vehicle at the early leaky tumour stage, monitored using both T1- and T2-weighted MRI throughout the study and analysed post-mortem using confocal microscopy (without staining) and light microscopy (with staining).

nanoparticle binding and chemotherapy release following internalisation [11]. Active targeting of nanomedicines to EphA2 in tumour proliferative cells can be driven by novel bispecific antibodies (BsAbs) that link the PEG arms of HBPs to the target tumour tissue [12], as we have previously demonstrated in brain tumour models [13]. Doxorubicin (Dox) is a potent chemotherapeutic which blocks topoisomerase II and intercalates DNA [14], and has shown efficacy against brain tumours in numerous studies [15–17]. Moreover, Dox is inherently fluorescent, allowing drug delivery and distribution in tissue to be monitored by various optical imaging techniques. When circulating as a free drug, Dox has been shown to cause serious off-target side effects in peripheral organs, with a key example being cardiomyopathy through mitochondriopathy [18].

In this work, we utilised a targeted nanomedicine approach for selective chemotherapeutic delivery to brain tumours where the Dox is formulated as a polymeric pro-drug. This model drug delivery system combined previous approaches comprising a PEGylated HBP with hydrazone bond-linked Dox and a BsAb engineered to contain two single chain variable fragments to produce an αPEG-αEphA2 construct (Fig. 1A). This design was proposed to target high grade brain tumours at a stage of enhanced crossing of the blood brain barrier (BBB), and specifically release Dox in the low pH environment of the tumour tissue [13,19–21].

An optimal method to measure brain tumour volume and 'leakiness' is magnetic resonance imaging (MRI). We have defined leakiness as leakiness of the vascular endothelium surrounding the tumour [13]. T2-weighted MRI can be used to visualise areas of the brain which have a higher density of water, which is ideal for identifying dense tumours. T1-weighted MRI on the other hand can be used in combination with a suitable small molecule contrast agent (e.g.: Magnevist® or Gadovist®) to measure the degree of leakiness associated with the BBB, which occurs most severely when brain tumours progress to include angiogenesis and BBB breakdown [22]. We have previously used this methodology to ascertain the optimal stage for delivery of nanomedicines to spontaneous tumours where the biology can be matched similarly to human tumours for understanding factors such as leakiness [13]. Specifically, it was determined that nanomedicine treatment of glioblastomas has increased potential for success when the HBPs are able to cross the BBB at earlier stages of leakiness [13].

Recent research has shown that tumour angiogenesis and leakiness are the strongest predictors of increasing severity (Fig. 1B) [13,23]. In this study we used T2-and T1-weighted MRI to longitudinally assess mice for brain tumour development (tumour volume) and BBB leakiness to inform the timing of systemic delivery of Dox-loaded nanomedicines at the early but leaky stage of tumour growth. Treatments comprised of either vehicle, free Dox, Dox conjugated to HBP, or Dox conjugated to HBP and functionalized with αPEG-αEphA2 BsAb (BsAb + HBP), were administered five times over 2.5 weeks (Fig. 1C). We found that high grade brain tumour growth slowed when treated within an early treatment window (based on "leakiness" of the BBB and subsequent accumulation into the tumour) by Dox-loaded HBP, or Dox-loaded HBP with BsAb, and that these nanomedicines cause a reduction in cancer cell prevalence, and an associated increase in apoptosis. Importantly, the HBP and BsAb + HBP also avoided cardiomyopathy, which was seen in mice treated with Dox alone. From this work we propose that BBB-permeable brain tumours should be treated as early as possible for optimal nanomedicine accumulation and treatment efficacy through apoptosis and slowing of growth.

2. Materials and methods

2.1. Materials

Chemicals were purchased from Sigma-Aldrich (Australia) unless otherwise stated. 4,4′-azobis (cyanovaleric acid) initiator (ACVA; Sigma-Aldrich) was recrystallized in methanol before use. Solvents including dichloromethane (CH_2Cl_2), tetrahydrofuran (THF), dimethylsulfoxide (DMSO), *n*-hexane, methanol, and acetonitrile were used dry where applicable and of reagent grade quality. Poly (ethylene glycol)monomethyl ether methacrylate (PEGMA, $M_n = 475$ g mol^{-1}, Sigma-Aldrich) and ethylene glycol dimethacrylate (EGDMA, Sigma Aldrich) were destabilized by passing them over a column of basic alumina and stored at −20 °C. Milli-Q water (18.2 MΩ cm^{-1}) was used throughout. 4-Cyano-4-(phenylcarbonothioylthio)pentanoic acid (PETTC) was synthesised following the procedure of Semsarilar et al. [24]. Cyanine 5 methacrylamide (Cy5 MA) was synthesised following the procedure of Fuchs et al. [25]. All nanomaterials were characterized using standardised reporting methods recommended by Faria et al. [26].

2.2. Nuclear magnetic resonance (NMR)

NMR experiments were conducted on a Bruker Avance 500 MHz high-resolution NMR spectrometer. Diffusion-weighted spectra (DOSY) were collected at a gradient strength (gpz6) of 50% for a minimum of 128 scans. Chemical shifts are reported as δ in parts per million (ppm) and referenced to the chemical shift of the residual solvent resonances ($CDCl_3$ ^{1}H: $\delta = 7.26$ ppm; DMSO-d_6 ^{1}H: $\delta = 2.50$ ppm). The resonance multiplicities are described as s (singlet), d (doublet), t (triplet), q (quartet), m (multiplet) or br (broad).

2.3. Size exclusion chromatography (SEC)

SEC was performed on a SEC-multi-angle laser light scattering (MALLS) chromatographic system consisted of a 1515 isocratic pump (Waters), a 717 autosampler (Waters), Styragel HT 6 E and Styragel HT 3 columns (Waters), 2414 differential refractive index detector (Waters) and a Dawn Heleos laser light scattering detector (Wyatt). THF was used as the mobile phase throughout with a flow rate of 1 mL/min. For effective light scattering analysis, the Cy5 fluorescence was first quenched by mixing 10 mg of polymer in 1 mL of THF along with a 4 mm^2 piece of silver foil. The solution was bubbled with oxygen for 20 min, then left sealed under this high-oxygen atmosphere until no blue colour remained (through overnight oxidation).

2.4. Ultraviolet–visible spectroscopy (UV–Vis)

UV–Vis was performed on a Nanodrop 2000C spectrophotometer (Thermo Scientific) using a quartz-glass pedestal with 1 mm path length. Absorbance maxima were recorded at 480 nm absorbance in triplicate for Dox and HBP-Dox, and concentrations of Dox per HBP were quantified relative to linear calibration curves of Dox standards. HBP Cy5 fluorescence was also checked using UV–Vis at 630 nm absorbance.

2.5. High-performance liquid chromatography (HPLC)

HPLC was carried out using a Thermo Dionex Ultimate 3000 HPLC equipped with a VWD-3100 variable UV–visible detector, a FLD-3100 fluorescence detector, a Thermo triple quad TSQ Quantum Ultra QqQ mass spectrometer and a reversed-phase C_{18} column (Phenomenex Kinetex 2.6u, 75 × 4.6 mm for Figure S4A, Figure S4B, Figure S4C; Synergi 4u Hydro-RP 80 A, 150 × 3 mm for Figure S4D. A gradient elution from 4% acetonitrile (MeCN) in 18.2 MOhm purified water (Milli-Q) containing 0.2% formic acid to 80% MeCN in Milli-Q water containing 0.2% formic acid over a time period of either 30 min or 15 min, with either a 200 or 400 μL/min flow rate respectively (Fig. 4A–C vs Fig. 4D). The gradient program was as follows, 10% buffer for 2 min, followed by a linear ramping to 100% B over 24 min, the gradient was held at 100% B for 1.5 min, returned to 10% B over 0.5 min, and held at 10% B for 2 min to re-equilibrate the column for the subsequent analysis. The loading purity of the HBP-Dox from free Dox was determined through measurement of the fluorescence using an excitation of 480 nm and emission detection of 560 nm. HBP Cy5 fluorescence was also

validated using 630 nm excitation and 650 nm emission spectra.

2.6. HBP dox release assay

Phosphate buffer solutions (PBS) with a pH at 7.4 and 5.5 were used to simulate physiological and endosomal conditions. PBS buffer 7.4 was acidified with the addition of diluted (0.1 M) HCl to form the PBS pH 5.5 solution. A Dox HCl calibration curve was created using nine concentrations made up in duplicate in PBS buffer pH 7.4 in a 48 well plate. A Tecan 200 Plate Reader was used to read the absorbance at 590 nm with 25 flashes each. 1 mg of HBP-DOX was dissolved in 1 mL PBS buffer 7.4 and added to a 3.5 kDa Snakeskin dialysis tubing. This was then placed in a sealed glass apparatus containing either PBS buffer 7.4 or 5.5 and stirred for 48 h at 37 °C. Aliquots of the dialysis solution (1 mL) were removed at predetermined time points and replaced with fresh buffer. The aliquots were measured using the same settings on the plate reader as the calibrations. The release studies were performed in duplicate.

2.7. PEGMA-co-TBMC-COOH HBP (1)

HBP synthesis was conducted using protocols previously published in our laboratory [7,27], and the reaction scheme is summarised in Figure S1. Briefly, PEGMA (0.5 g, 1.05 mmol), Cy5 MA (4.3 mg, 6.58 μmol), EGDMA (0.013 g, 65.8 μmol), BOC-protected hydrazide methacrylate (TBMC, 0.053 g, 0.263 mmol), ACVA, 3.7 mg, 65.8 μmol) and PETTC (0.0223 g, 13.2 μmol) were dissolved in THF (0.6 mL) and degassed by nitrogen sparging for 20 min in a Schlenk ampoule. The resultant solution was then reacted at 80 °C for 24 h. The polymer was then precipitated into *N*-hexane, decanted and dried under vacuum overnight. The resulting oil was then re-dissolved in Milli-Q water, dialysed against Milli-Q water for 4 d in 10 kDa molecular weight cut-off Snakeskin® tubing (ThermoFisher), then lyophilised overnight to yield a blue viscous oil (>90% conversion, 540 mg). ^{1}H NMR (500 MHz, DMSO-d_6): δ 7.2–7.0 ppm (m, Ar, 1H), 4.02 ppm (s, $COOCH_2$, PEGMA, 42H), 1.45 ppm (s, $(CH_3)_3OC(O)NHNH$, 52H). SEC: $M_{n,SEC\text{-}MALLS} = 48$ kDa; $Đ_M = 3.23$.

2.8. PEGMA-co-TBMC-N_3 HBP (2)

HBP2 was generated by mixing HBP1 (100 mg, 7.14 μmol) with 2-azidoethanol (7.2 mg, 71 μmol), for 10 min then 1-ethyl-3-(3-dimethylaminopropyl)carbodiimide hydrochloride (EDC-HCl, 2.7 mg, 1.4 μmol) in CH_2Cl_2 for 20 min on ice, followed by adding 4-dimethylaminopyridine (DMAP, 87 μg, 71 nmol) in CH_2Cl_2 for 24 h. The resultant HBP2 was purified as above, yielding >95% conversion (95 mg). The addition of the azide group was verified by Fourier-transformed infrared (FTIR) with an Agilent CARY 630 FTIR spectrometer, showing a peak at wavenumber 2100 cm^{-1}.^{1}H NMR (500 MHz, $CDCl_3$): δ 4.02 ppm (s, $COOCH_2$, PEGMA, 1.45 ppm (s, $(CH_3)_3OC(O)NHNH$).

2.9. PEGMA-co-hydrazide-N_3 HBP (3)

HBP3 was generated by deprotecting the tert-butyloxycarbonyl (BOC) protecting groups from HBP2 with 20% trifluoracetic acid (TFA) in CH_2Cl_2 for 24 h, then purified as above, yielding >81% conversion (77 mg).^{1}H NMR (500 MHz, $CDCl_3$): δ 4.02 ppm (s, $COOCH_2$, PEGMA, 8.0 ppm (s, Doxorubicin).

2.10. PEGMA-co-hydrazone-DOX-N_3 HBP (4)

HBP4 (the HBP used in this study) was then generated by mixing 262 mg HPB3 with 26.2 mg Dox in 1 mL anhydrous methanol and a drop of glacial acetic acid for 24 h, and purified by dialysis for 2 weeks and with 10% methanol and ~0.1% sodium bicarbonate included in the MilliQ water dialysis buffer, yielding >77% conversion.

2.11. BsAb synthesis

BsAbs against EphA2 were expressed in and purified from Chinese Ovarian Hampster (CHO) cells as previously described [12], and the process is briefly described here. Genes encoding the BsAbs were synthesised by GeneArt (Invitrogen). The BsAb genes were cloned into a mammalian expression plasmid (pcDNA 3.1 (+), Invitrogen) using *Hin*dIII and *Not*I restriction sites, adding a 6 × His motif (for affinity purification) and a c-Myc epitope at the *N*- and C-termini, respectively. Plasmid DNA (2 μg/mL) was complexed with polyethylenimine-Pro (PolyPlus) in Opti-Pro serum free medium (Life Technologies) at a DNA (μg) to PEI (μL) ratio of 1:4 (w:v) for 15 min before transiently transfecting suspension adapted CHO–S cells (3×10^6 mL^{-1}). Cells were grown in chemically defined CHO medium (CD-CHO, Life Technologies) at 37 °C, 7.5% CO_2 with shaking (130 rpm) for 6 h, before adding 7.5% CD-CHO Efficient Feed A (Life Technologies), 7.5% CD-CHO Efficient Feed B (Life Technologies) and 0.4% anti-clumping agent (Gibco), and culturing at 32 °C, 7.5% CO_2 with shaking for 7–14 days. Cells were cultured until their viability reduced below 50% as measured by trypan blue exclusion. Following expression, BsAbs were purified by pelleting cells by centrifugation (5250 rcf, 30 min), filtering supernatant through a 0.22 μm membrane (Sartorius) and purifying with a 5 mL HisTrap excel column (GE Healthcare). BsAbs were eluted with 20×10^{-3} M sodium phosphate, 500×10^{-3} M sodium chloride and 500×10^{-3} M imidazole pH 7.4. Alternatively, a 5 mL Protein L column was used, with BsAbs eluted using 100×10^{-3} M glycine pH 3.0. Following buffer exchange and size exclusion chromatography as described previously [12], BsAbs were filtered through 0.22 μm membranes and stored at 0.25–0.60 mg mL^{-1} in buffer containing 20×10^{-3} M sodium phosphate and 500×10^{-3} M sodium chloride at pH 7.6.

2.12. Animal model and tumour induction

All experiments were approved by the University of Queensland Animal Ethics Committee and followed the Australian Code of Practice for Use of Animals for Scientific Purposes (QBI/356/17/UQ, AIBN/142/19/UQ). Pten^{tm2MAK}; Rb1^{tm2Brn}; Trp53^{tm1Brn}; Tg (GFAP-cre/Esr1*,-lacZ) BSbk mice [26,27] were injected intraperitoneally with 200 mg/kg tamoxifen (Sigma Aldrich) in corn oil (Sigma Aldrich), weekly over 3 consecutive weeks starting from 4 to 6 weeks of age. Mice with tamoxifen-induced deletion of tumour suppressor genes *Pten*, *Rb1* and *Trp53* were monitored daily and were euthanized between 180 and 260 days post-tamoxifen injection, reaching morbidity due to tumour-related symptoms. Animals were excluded for the treatment study if presenting with non-brain tumour malignancies.

2.13. Evaluation of brain tumours using MRI

For MRI scanning, mice were anaesthetised using 2.5% isoflurane until in deep sleep and maintained under 1–2% isoflurane with respiratory monitoring and body temperature heating. Mouse brains were monitored weekly using T2-weighted MRI to check for brain tumour masses in a Bruker 7 T ClinScan with Siemens VB17 software (axial: 19 × 0.6 mm slices, field of view (FOV) = 25 × 18.74 mm, in-plane resolution = 98 × 98 μm, repetition time (TR) = 2800 ms, echo time (TE) = 50 ms, averages = 2, acquisition time = 5 min, 19 s; sagittal: 19 × 0.6 mm slices, FOV = 25 × 18.74 mm, in-plane resolution = 98 × 98 μm, TR = 2800 ms, TE = 50 ms, averages = 2, acquisition time = 5 min, 19 s; coronal: 30 × 0.6 mm slices, FOV = 25 × 25 mm, in-plane resolution = 98 × 98 μm, TR = 4404.9 ms, TE = 50 ms, averages = 2, acquisition time = 8 min, 22 s). Once distinct brain tumour masses were detected with T2-weighted MRI, the brain tumour BBB leakiness was investigated using T1-weighted MRI with contrast agent. Mice were injected with 200 μL of 25% Gadovist® 1.0 in saline through a cannula in the tail vein and scanned axially using T1-weighted gradient dual echo sequences every 3 s for 600 s in total (200 measurements, flip angle = 25°, 5 × 1

mm slices, FOV = 30 × 30 mm, in-plane resolution = 234 × 234 μm, TR = 50 ms, TE = 3.5 and 6 ms. BBB leakiness was also confirmed in a preliminary mouse using multi-spectral optoacoustic tomography (MSOT). Horos (v3.3.6) and Slicer (v4.10.1) software were used to analyse MRI DICOM files, with the Horos dynamic contrast enhancement (DCE) tool plugin (v2.2) used to quantify gadolinium permeability in two-dimensional circular regions of interest (ROIs) in gradient echo scans.

2.14. Treatment of brain tumours with nanomedicine

Mice were intravenously injected with either saline (0.9% sodium chloride, Baxter) as a vehicle control, free Dox in PBS (4.5 mg/kg), Dox-loaded hyperbranched polymer (HBP), or HBP with 1:1 αEphA2 BsAb (BsAb + HBP) at a dose of 4.5 mg/kg of Dox into the lateral tail vein. For BsAb + HBP treatment, the HBP and αEphA2 BsAb were incubated at a 1:1 ratio at room temperature (RT) for 1 h prior to injection. The tumour volume was measured using T2-weighted imaging, and the longest diameter in any plane was measured as per Response Evaluation Criteria in Solid Tumours (RECIST) guidelines [28]. Measurements were taken every 3–4 days up to the final treatment time point, and then followed-up with further imaging at later time points as the mice started to show worsening symptoms.

2.15. Collection, sectioning and histological evaluation of mouse brains and hearts

Mice were given a peri-lethal intraperitoneal injection of 100 mg/kg sodium pentobarbital in PBS, then transcardially perfused with 12 mL saline solution, followed by 12 mL ice-cold 4% paraformaldehyde (PFA) in PBS. The brain, heart and liver were then immersion fixed in 4% PFA in PBS at 4 °C for 24 h. Brains and hearts were embedded in 4% noble agar in PBS (Sigma Aldrich), then sectioned at 50 μm using a V1000S vibratome (Leica). Sections were mounted onto Superfrost plus microscope slides in DABCO mounting media, and sealed with nail polish. Separate brain sections were stained with terminal deoxynucleotidyl transferase dUTP nick end labelling (TUNEL) assay kit following manufacturer's instructions (Abcam, ab206386), and sealed with ultramount mounting media (ThermoFisher). Heart and brain tissue sections were stained using haematoxylin (8 min) and 1% eosin (30 s), dehydrated and mounted with ultramount (ThermoFisher).

2.16. Microscopy

Spinning disk confocal images were acquired on a spinning disk confocal microscope (Diskovery; Andor Technology, UK) built around a Nikon Ti-E body (Nikon Corporation, Japan) and equipped with two Zyla 4.2 sCMOS cameras (Andor Technology), a Nikon Plan Apochromat 20x/0.75 NA air objective, Nikon Plan Apochromat Lambda 60x/1.4 NA oil objective and controlled by Nikon NIS-Elements AR software. Images were scanned as 6 × 6 stitched 20x tiles with 10% overlap, or 25 slice Z-stacks at 0.9 μm step intervals at 60x. DAPI was excited with a 405 nm laser, Dox was excited with a 488 nm laser, tdTomato was excited with a 594 nm laser, and Cy5 was excited with a 640 nm laser, with corresponding filter sets. Colour brightfield images of TUNEL apoptosis staining and heart ventricle sections were conducted on an epifluorescence axio imager microscope (Zeiss) with ZEN blue software, using a TL LED lamp, Axiocam 512 camera and EC Plan-Neofluar 10x/0.45 NA air objective and 5x/0.16 NA air objective with 4 × 4 tiles respectively. TUNEL DAB staining was quantified by thresholding the red channel to 2500 Gy levels in ImageJ, and measuring the percentage area to get the apoptotic index.

2.17. Multispectral optoacoustic tomography (MSOT)

For optoacoustic imaging, an MSOT inVision 256-TF small animal imaging system (iThera Medical, Munich, Germany) was used. The mouse was horizontally positioned in a holder (iThera Medical) under 2% isoflurane anaesthetic and wrapped in a thin polyethylene membrane with ultrasound coupling gel applied to provide contact between the animal and the membrane of the animal holder. The mouse head was z-translated through the imaging plane in 0.5 mm oversampling steps using a linear stage control to acquire a stack of 2D axial images over the brain region which in turn allowed for optimal three-dimensional (3D) rendering. 10 frames at each of the following wavelengths were acquired: 680, 715, 730, 760, 765, 770, 800 and 845 nm. The images were reconstructed using a model-based algorithm and processed using linear spectral unmixing to identify the signal of oxygenated and deoxygenated haemoglobin.

2.18. Pharmacokinetics study using a fluorescence in vivo imaging system (IVIS)

Twenty-three C57 mice were used to determine the pharmacokinetic profile of the targeted and untargeted HBP in peripheral and brain organs compared to free Dox and vehicle (ethics approval was received from the University of Queensland animal ethics committee, ethics approval number: AEC440/20). Mice were injected with the required material (4.5 mg/kg DOX equivalent) and then sacrificed at 24 hrs post administration. Tissues were collected and rinsed in saline to remove contributions from blood before being imaged using the same imaging imaging protocol. Cy5 signal was unmixed before ROI imaging anylsis was conducted to semi-quantitatively determine biodistribution. A spectral unmixing method specific to Cy5 was employed whereby four images were captured and overlaid with photographs, in both supine *in vivo*, prone *in vivo* and organ *ex vivo* data sets. The excitation/emission spectra in nm were 560/670, 580/670, 600/670, 620/670.

2.19. Sodium dodecyl-sulfate polyacrylamide gel electrophoresis (SDS-PAGE)

SDS-PAGE was run on a Bolt™ 4–12%, Bis-Tris protein gel (Invitrogen) following manufacturer's protocol. 1 mg/mL HBP was incubated in human and mouse serum respectively over 60 h at 37 °C, then diluted 1 in 10 and 5 μL loaded onto the gel, while in a separate lane 5 μL of 1 mg/mL Cy5-amine labelled positive control polymer (HBP2) in saline was loaded. Gel images were captured on a Bio-Rad ChemiDoc MP using settings for Cy5 detection. The protein standard used was Precision Plus Kaleidoscope (Bio-Rad).

2.20. Data collection and statistical analysis

All data was collected and analysed according to the guidelines for Minimum Information and Reporting in Bio-Nano Experimental Literature (MIRIBEL) in order to maintain the best reporting of reproducible and reliable data [26]. Groups were compared by one-way ANOVA with a Tukey's multiple comparison test using Graphpad Prism (v8) software. All bar graphs indicate mean + standard error of the mean.

3. Results & discussion

3.1. Establishment of glioma mouse model

To study whether nanomedicine is viable to treat aggressive brain cancer, we used a mouse model which includes three signature post-natal tumour suppressor mutations, in RB1, PTEN and TP53, and are induced at a 4–6 weeks of age in GFAP-positive cells through a Cre-lox recombination system. Mutations in RB1 are found in up to 78% of patients with GBM, whilst PTEN and TP53 mutations are found in up to 87% [29,30]. This model begins to develop a leaky-stage GBM at approximately 100–200 days after induction of the mutations with tamoxifen and expresses tdTomato in mutated GFAP-expressing cells,

making it ideal for investigating brain tumour structure using confocal microscopy by exciting in the near-far-red (594 nm) channel, which also later avoided overlapping fluorescence from Cy5 (640 nm channel), and doxorubicin (488 nm channel) [13,26].

3.2. Generation and characterisation of a functional HBP and αPEGMAαEphA2 BsAb

For this study we desired a biocompatible nanomedicine, capable of being monitored via fluorescence for tissue evaluation, able to carry chemotherapy (Dox) and be targeted to tumour specific marker EphA2, in order to treat brain cancer more effectively and produce less side effects than standard chemotherapy (Fig. 1). We utilised well established RAFT polymerisation to produce a multifunctional polymeric nanomaterial core of methacrylate monomers, generating HBP1, and incorporated an azide group for further post-modification in downstream PET applications to make HBP2 (Figure S1) [7,8]. Notably, we incorporated TBMC for drug loading (post-polymerisation), and Cy5 was labelled at a 0.1 ratio for fluorescence detection (Fig. 1A; stability of Cy5 conjugation in buffer at pH 7 and in serum shown in Figure S3D). PEGMA was the major monomer incorporated to provide biocompatibility, while EGDMA was included to provide branch points between chains. As shown in Table 1, a 48 kDa Dox-loaded HBP with an average of 3.5 arms per polymer was successfully generated, and chemical properties measured by GPC-MALS and NMR spectroscopy (Figure S2). The removal of the TBMC BOC group from HBP2 was confirmed by disappearance of the peak at 1.4 ppm in proton NMR (Figure S2), making HBP3. Doxorubicin was also then reacted at a 0.1 ratio by weight, and analytical HPLC with a fluorescence detector ($\lambda_{excitation}$ 480 nm $\lambda_{emission}$ 560 nm) was used to assess Dox conjugation, and showed ≥94% purity (Figure S3) for HBP4. For clarity through the remainder of the manuscript we will refer to HBP4 as 'HBP' as this is the material administered in all cases. The final characteristics of the HBP nanomedicine core included fluorescence detectability, pH-sensitive Dox release, and immune evasion through incorporation of PEGMA. This was further functionalized to provide antigen specificity through the incorporation of a BsAb (Fig. 1). The BsAb that was generated consisted of two single chain variable fragments (scFvs) tethered by a flexible glycine4-serine linker, making it a total size of 54 kDa and being specific to both PEG (the primary HBP component) and EphA2 [12].

These materials are a well described class of nanomedicine, of 5–10 nm in size [7,31] with well understood biodistribution properties, long circulation times (>12 h blood half-life) [32], and which incorporate chemotherapeutic Dox as a pro-drug that is stable under physiological conditions but releases within 24 h upon encountering the acidic lysosomal environment [33] (Figure S3B).

3.3. Diffusivity of targeted and untargeted HBP into leaky stage brain cancer tissue

Accessibility of circulating nanomedicine to the tumour is key in effective therapeutic delivery, particularly for hard-to-reach tumours such as those growing in the brain. Recent work has demonstrated analogous materials were able to cross the BBB at various stages of glioblastoma [13], showing comparable biodistribution and pharmacokinetics in this model. As a preliminary study we correlated BBB permeability with clinically relevant T1-weighted gradient echo MRI using Gadovist® (Gad) as a diagnostic readout. The MRI offered insight into the progressive leakiness of solid tumours (in terms of extravasation of molecules from the bloodstream into the tumour) and was correlated with vascular imaging acquired using multispectral optoacoustic tomography (MSOT) (Fig. 2A). We applied the same criteria as discussed in Houston et al. 2020 [13] to classify tumours as 'leaky' or not. It was found that in mice with a gadolinium-permeable brain tumour, both the HBP and BsAb + HBP nanomedicines were able to enter and accumulate in the tumours through the leaky BBB over a monitoring period of 48 h (Fig. 2B). The stability of the Cy5-conjugate was confirmed by incubation of the HBP in serum over 6 days at 37 °C, followed by SDS-PAGE (Figure S4). This also supported our recent work showing high penetration of nanomedicines at similar stages of disease progression as demonstrated by gadolinium permeability, although similarly we did not observe any effect of the nanomedicine in reducing leakiness [13]. Using this as a key rationale for the treatment study design, we aimed to wait until the glioblastomas showed gadolinium permeability before initiating the treatment regime. Similar to clinical cases of brain cancer, the inducible genetic mouse model used here results in rapid and spontaneous tumour development [26,27], being temporally, spatially and biologically heterogeneous, making this a useful primary brain tumour model in which to assess nanomedicine treatment of glioblastoma. While this model provides unique advantages (for example understanding BBB changes), a major disadvantage compared to other models is its variability in tumour starting point and severity, which produced challenges regarding therapeutic efficacy assessment. Therefore we proceeded to do a small-scale treatment study in a personalised monitoring, unique case-by-case approach.

Table 1
Physicochemical properties of the HBP.

	Average arms per polymer	Average HBP molar mass	Average molar mass per arm	Doxorubicin loading purity	Cy5/HBP (degree of functionalisation)
HBP	3.5	48.1 kDa	13.5 kDa	≥94%	10%

3.4. Effect of targeted and untargeted HBP on slowing brain cancer growth

Many murine nanomedicine studies reported in the literature aim to achieve regression in xenografts of immortalised cell lines, however we aimed to use a model which can assess preclinical aspects including variable tumour initiation, growth and effect on the surrounding brain tissue. While this allowed a more universal evaluation of how the treatment groups perform holistically as a therapy, a disadvantage of this model is that it is difficult to deconvolve the various parameters that lead to successful treatment outcomes (owing mainly to the inability to control for the heterogeneity in pathophysiology of the disease in these models). For example, the variability in location and aggressive nature of the tumours makes conventional measurements of survival (for example) less informative in the context of this study and so in our data we were more focused on investigating how the drug delayed tumour progression on a case-by-case basis. Hence, the aim of this part of the study was to test a proof-of-concept of the treatment efficacy of free Dox, Dox-loaded HBP and Dox-loaded HBP that was targeted to receptors present on tumour tissue using a bispecific antibody (BsAb + HBP) compared to vehicle controls. In all cases treatment was only initiated once the tumours showed gadolinium leakiness, as classified in our previous work [13]. It was found that when treatment with Dox or HBP was initiated at a large (late-stage) tumour volume (which we defined as greater than 50 mm^3), tumour growth continued at a slower but steady rate, compared to animals with similar size tumours treated as vehicle controls (Fig. 3A). However, when treatment of the tumours commenced at a small (early-stage) volume stage (which we defined as ~5–50 mm^3), whilst also being leaky, the BsAb + HBP appeared to have the greatest effect on slowing tumour growth, followed by the HBP (trending, $p = 0.052$), as compared to the Dox and vehicle treated groups (Fig. 3B). For the larger tumours, there was only a difference in growth rate between the BsAb + HBP and vehicle groups (probably owing to the fact that at this stage the tumours were significantly progressed as to be less affected by treatments with HBP alone, and a limited number of mice were treated at this stage). The overall increased effectiveness of the BsAb + HBP treatment compared to Dox could be attributed to improved

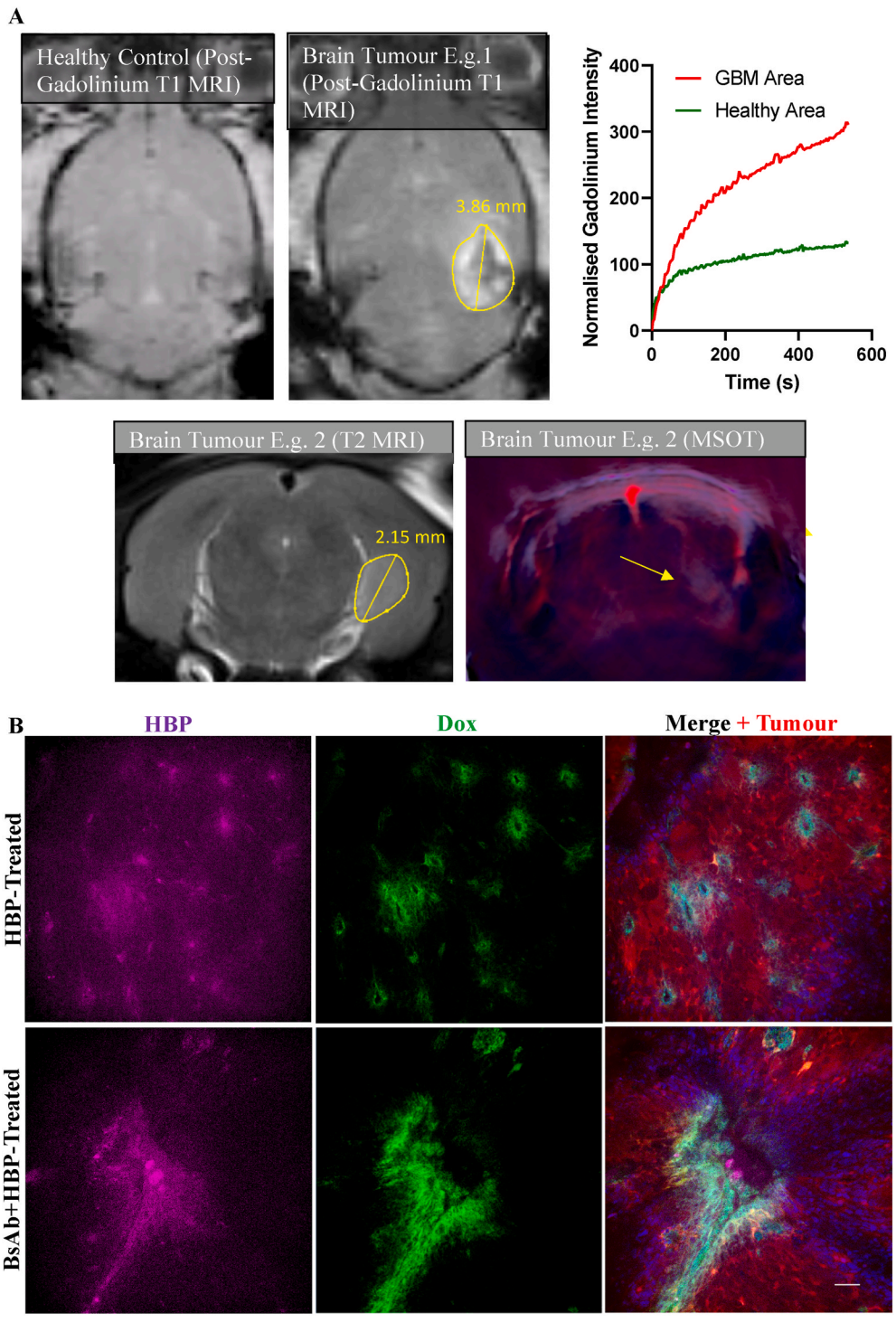

Fig. 2. A) Gadolinium injection with T1-weighted gradient dual echo sequences (axial view) shows leakiness of negative (healthy) control brain area over time, compared to mouse brain area with leaky stage hippocampal tumour. Red line represents increasing gadolinium signal over time in tumour area (hippocampal), while green line represents relatively flat control brain area gadolinium signal. Yellow arrow shows oxygenated (red) and deoxygenated (blue) blood signal in tumour area, as visualised by MSOT (coronal view), and the same tumour was also visualised by T2-weighted MRI (coronal view). Tumour width was 1.3 mm. **B)** Spinning disk confocal microscopy showing the intra-tissue distribution of HBP and BsAb + HBP, and independent Dox distribution 48 h following intravenous injection; tumours were first shown to be perfused with Gadolinium by MRI to confirm "leakiness". HBP-Cy5 is shown in magenta, Dox is shown in green, tdTomato tumour area is shown in red, and DAPI is shown in blue. Tumours showed variable fluorescence intensities (densities) and uptake. Scale bar represents 100 μm. (For interpretation of the references to colour in this figure legend, the reader is referred to the Web version of this article.)

sustained release of Dox into the leaky tumour area following retention of the targeted nanomedicine within the tumour and subsequent pro-drug activation (hydrazone cleavage and drug release) [21]. The proliferative niches in which the tumours predominantly grew in the brain included the hippocampus, thalamus, hypothalamus, striatum, basal ganglia and subventricular caudate putamen (Figures S5-S7). Taking all of these observations together, it was apparent that the HBP and BsAb + HBP slowed tumour growth throughout the continually leaky period, despite the variable and spontaneous location of the tumour. These promising initial results give understanding of how the HBPs and BsAbs act as drug delivery systems for brain cancer, and they could be expected to be follow similar trajectories in future clinical studies.

Our previous study demonstrated that the EphA2 targeted nanomedicine showed enhanced accumulation in the tumour tissue by PET. In this study, we were monitoring intratumoral distribution by microscopy of tissue slices and while it was not possible to evaluate whole tissue accumulation enhancement by this method, a qualitative comparison of relative uptake between the nanomedicines could be made. Nonetheless, the preliminary therapeutic study provided did show that the targeted nanomedicine was trending towards a more significant efficacy than the untargeted nanomedicine (biodistribution data for other

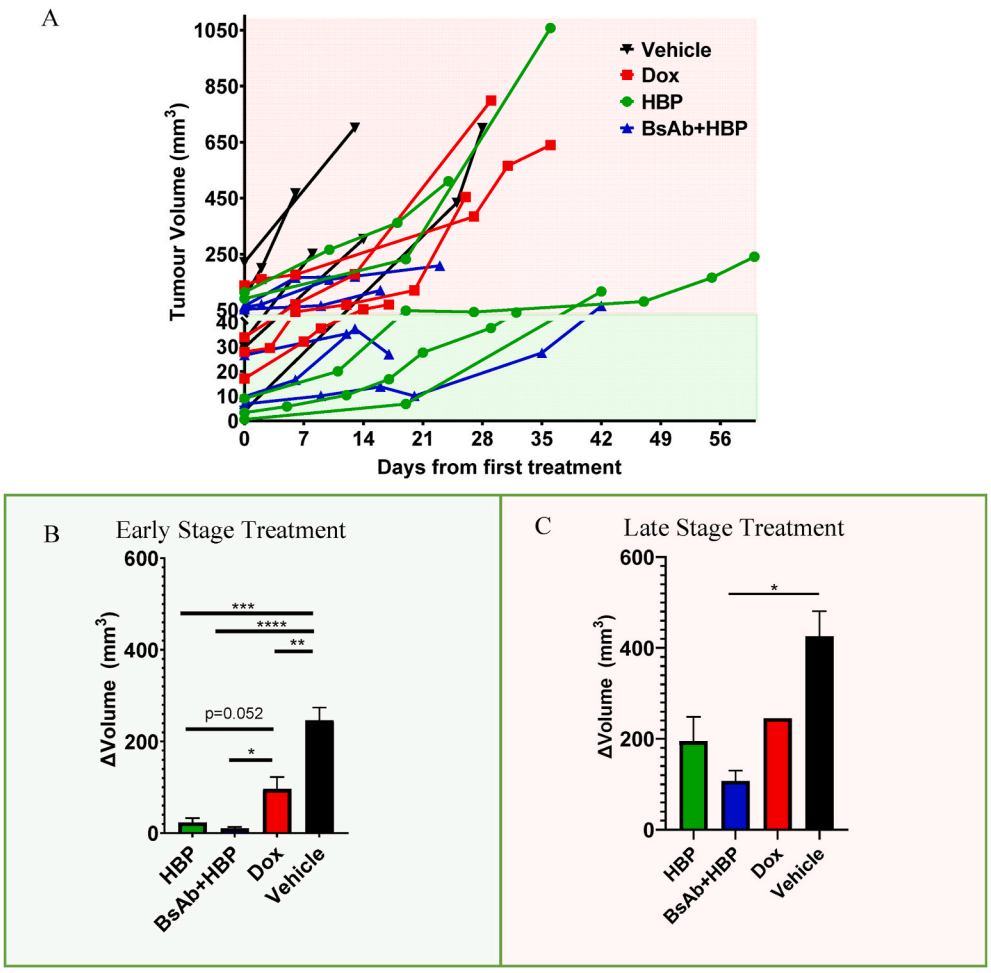

Fig. 3. Pilot efficacy of nanomedicine treatment. T2-weighted MRI and RECIST criteria were used to measure individual brain tumour volumes over time from first treatment. A) Tumour volumes were measured by MRI for each treatment cohort for tumours where therapy was commenced at an early or late stage. Brain tumour growth prevention was most pronounced when HBP and BsAb + HBP treatment was started at the early stages of growth, at less than 50 mm^3 in volume (green highlighted area). Dox and HBP treatment had a limited effect on tumour growth when treatment was started at large (>50 mm^3) tumour volume (red highlighted area), while BsAb + HBP had the strongest effect at the later larger stage. B) In the small tumours, volume of growth from beginning to end of the treatment period (Day 18) shows a maximal growth rate in the vehicle control group, followed by the Dox-treated group (n = 3), *p < 0.05, **p < 0.01, ***p < 0.001, ****p < 0.0001 one-way ANOVA with Tukey's post-hoc test. The BsAb + HBP group had the lowest growth rate, which was significantly lower than dox-treatment. C) In the limited number of larger starting point tumours, there appeared to be less difference in growth evident over the treatment period between BsAb + HBP and vehicle. The limited mouse numbers in this group (n = 1–3) was due to the spontaneous nature of the genetic glioblastoma model, and ~25% of mice were excluded after developing peripheral non-GBM tumours. A number of mice were euthanized at relatively smaller brain tumour volumes due to the development of severe endpoint symptoms such as breathing difficulties. (For interpretation of the references to colour in this figure legend, the reader is referred to the Web version of this article.)

organs shown in Figures S9-S10).

While this immunocompetent model offers insight into how the tumours develop in a spontaneous manner, the rapid tumour growth also has the consequence of being detected by imaging at later stages in development; this led us to stratify the brain tumours based on definable clinical stages. Although this led to a reduction in n-number for the comparison groups, a key expected finding of this study was that the large (>50 mm^3) leaky stage brain tumours responded with a less pronounced effect than the smaller (<50 mm^3) leaky stage tumours (Fig. 3). Although the sporadic and spontaneous growth response of this complex tumour model led to variability in the number of mice in each stratified cohort, the extensive imaging performed in this study showed that a BsAb + HBP targeted nanomedicine treatment is markedly improved compared to untargeted doxorubicin-only treatment (Fig. 3C). Moreover, irrespective of whether the mice were treated at early or late-stage tumour growth, the observed trends of HBP and BsAb + HBP being superior to doxorubicin and vehicle treatment groups were the same (Fig. 3).

3.5. Intratumoural distribution of nanomedicine and treatment area

One of the key factors that is considered to drive effectiveness of nanomedicines is their ability to penetrate tumour tissue to deliver therapeutic payloads [34]. Our recent work has shown good penetration of nanomedicines into brain tumour tissue if the tumour exhibits gadolinium permeability (what we consider as leakiness), and an improvement of BBB crossing with EphA2 BsAb targeting (0.3–3.3% injected dose range) [13]. In this study, MRI provided information on the disease state and we were able to measure therapeutic potential by investigating individual responses to drug administration; however, a more nuanced understanding of nanomedicine accumulation and consequent drug delivery is key to further progression of these materials as potential nanotherapeutics for brain tumours. To further evaluate the efficacy and accumulation of the nanomedicine treatments in the tumour microenvironments, tissue was processed and analysed with and without staining for apoptosis. Treated tumour microenvironments within brain tissue slices were first investigated using spinning disk confocal microscopy to investigate the localisation of the different fluorescent components in the delivery system and tissue; tumour astrocyte tdTomato (red), Dox (free drug or HBP conjugated; green), and Cy5 labelled HBP (magenta) (Fig. 4). Images were acquired following repeat intravenous administration of the different treatments until morbidity, after which the tumours were removed for analysis. Our analysis thus represents the distribution of nanomedicine components following prolonged longitudinal treatment. Areas of tumour regression were shown by a lack of tdTomato (red), and this typically corresponded to areas where Dox (green) was more intense. This is most clearly exemplified in mice that were treated with Dox alone that had low Dox signal and higher amounts of tdTomato, compared to animals treated with Dox-loaded HBP. In the latter, an approximate 10–50 μm radial

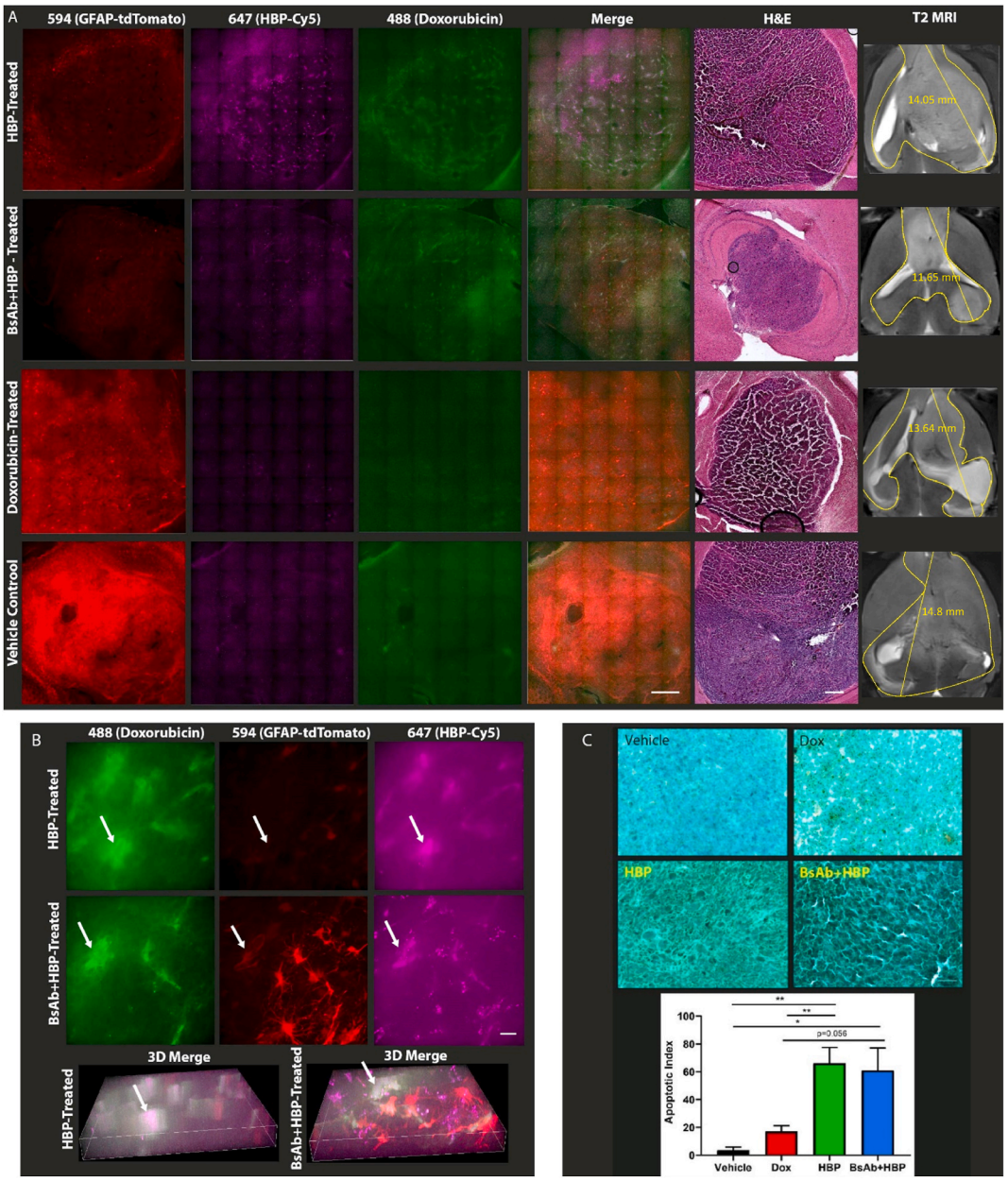

Fig. 4. A) Spinning disk confocal microscopy of treated brain tumour area shows relatively denser signal for tumour marker tdTomato (red) in vehicle control and Dox treated cases, compared to the BsAb + HBP and HBP treated cases. Dox is shown in green, and HBP-Cy5 is shown in magenta. There was no Dox signal seen in Dox-treatment above vehicle control background level, whereas both HBP and BsAb + HBP treatment showed a release of Dox into the tumour. Haematoxylin and eosin (H&E) staining showed slightly different morphologies between the treated tumours, with vehicle control showing highly dense and heterogeneous growth, similar to Dox-treated, whereas HBP-treated and BsAb + HBP-treated tumours appeared to show a larger healthy (pink) area, indicating lower density. Tumour area was also visualised with T2 MRI *in vivo* immediately prior to sacrifice. Scale bars represent 500 μm. B) Higher magnification maximum projection images of 25 slice Z stacks (0.9 μm space between each slice) show damaged tumour area corresponding to areas of HBP-mediated Dox release (arrow). The Dox appears to be released from areas of HBP accumulation within the tumour. Scale bar represents 20 μm. C) Terminal deoxynucleotidyl transferase dUTP nick end labelling (TUNEL) 3,3′-diaminobenzidine (DAB) staining shows higher apoptosis in HBP and BsAb + HBP treated tumour areas compared to vehicle and Dox treatment ($n = 3–4$) $^{*}p < 0.05$, $^{**}p < 0.01$, $p = 0.056$ trending, one-way ANOVA with Tukey's multiple comparison test. Sections were stained with DAB to indicate apoptosis, and counterstained with methyl green whereby yellow-green indicates lower pH. Darker red-black areas indicate fragmented DNA. Scale bar represents 100 μm. (For interpretation of the references to colour in this figure legend, the reader is referred to the Web version of this article.)

area around vasculature is observed with Dox signal release and absence of tdTomato (Fig. 4A and Figure S8). High magnification 3D images of these areas found instances of an outward diffusing front of Dox signal in the absence of signal attributed to HBP, suggesting release of the drug from the nanocarrier (Fig. 4A). This led to the death of cancerous tdTomato-expressing cells in the majority of cases. Furthermore, tumours treated with HBP and BsAb + HBP showed a greater amount of apoptosis compared to vehicle control and Dox-treated brain tumours (Fig. 4B), indicating that the higher ongoing Dox release by HBP has an enhanced effect on suppression of local brain tumour growth compared to freely circulating Dox. Presumably, this is due to enhanced accumulation of the drug in the tumour tissue when delivered by the nanomedicine. This was also supported by haematoxylin and eosin (H&E) staining of tumour tissue (Fig. 4A), which indicated a lower density of tumour tissue in the HBP and BsAb + HBP treated groups compared to Dox and vehicle treated groups. Despite high tumoural EphA2 receptor

expression previously shown in this model [13], there was no significant difference in the efficacy or response of the tumour to administration of BsAb + HBP or HBP alone, suggesting that accumulation in tumour tissue and release of Dox occurred independent of whether targeting ligands were used or not, or that any increased accumulation above untargeted levels did not induce any strong cumulative effect in this model. Similar to previous studies of analogous materials in our group, the biodistribution profile showed minimal uptake of either targeted or untargeted nanomedicine into the wild-type brain (which was also verified using confocal microscopy), and similar accumulation in the kidneys, liver, lungs and gut, whereas Dox was largely expelled from the system by 4 and 24 h (Figure S9, Figure S10). As evidenced in Fig. 4, the polymers showed a high accumulation within leaky tumour tissue, which matches our recently published data and previous studies.

3.6. Effect of different treatments on cardiotoxicity in mice

While effective treatment is desirable, one of the key drawbacks of conventional chemotherapy is dose-limiting toxicity. We therefore wanted to investigate whether the nanomedicine formulation was able to mitigate Dox-associated systemic side-effects. Doxorubicin is well-known to cause significant cardiotoxicity in patients when administered systemically, and this leads to dose-limited therapeutic challenges with the drug. Accordingly, at the conclusion of the therapeutic study, cardiac tissue was collected, sectioned and visualised using H&E staining to assess tissue damage. We observed cardiotoxicity in Dox-treated

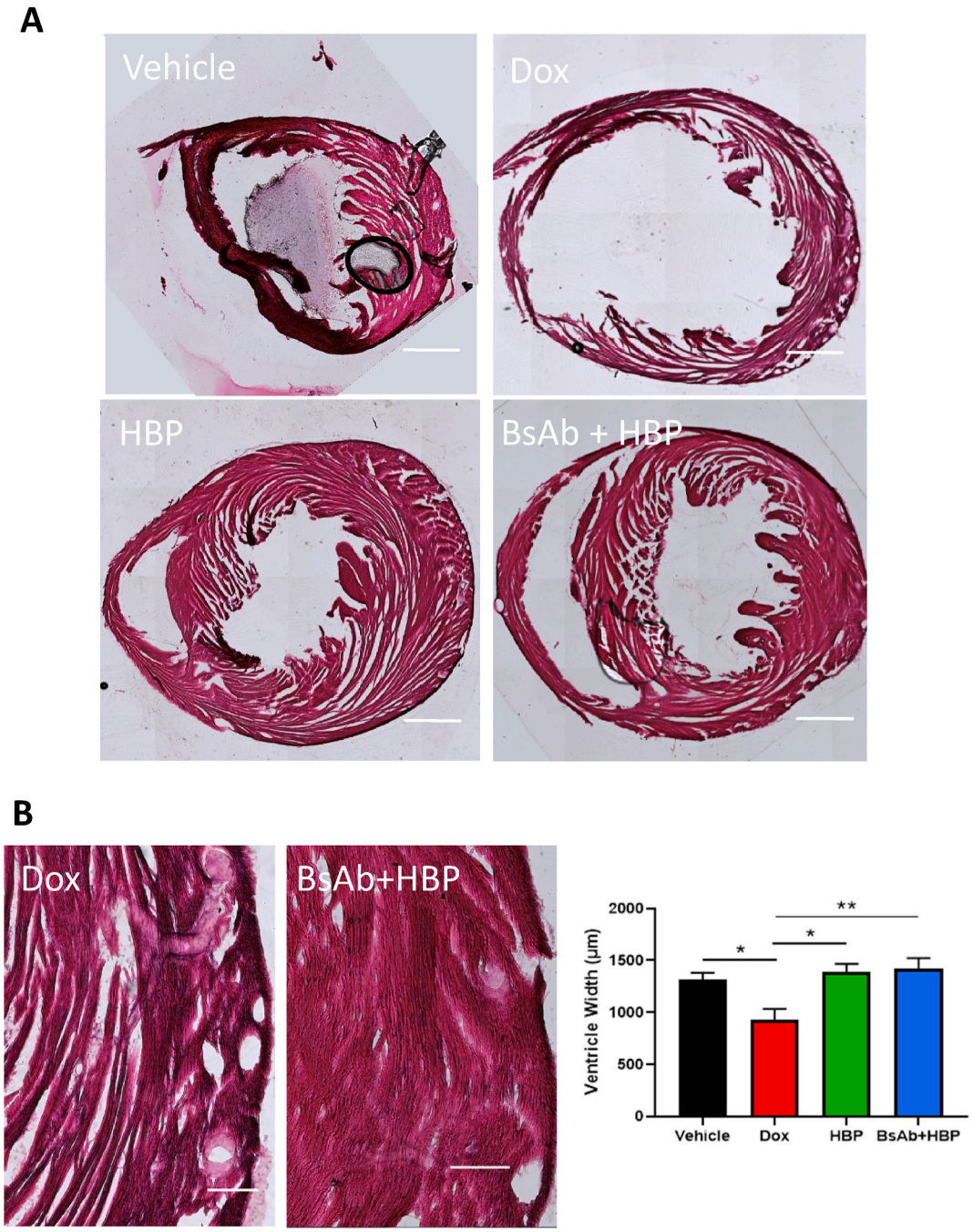

Fig. 5. Heart left ventricular width was thinner following Dox treatment, compared to vehicle control, HBP and BsAb + HBP treatment (n = 4–5) *p < 0.05, **p < 0.01, one-way ANOVA with Tukey's multiple comparison test. Tissue was stained with haematoxylin and eosin. Scale bar represents 1000 μm for A and 200 μm for B.

mice under the therapeutic regime investigated, which was not apparent in the vehicle control nor targeted or untargeted nanomedicine treated groups (Fig. 5). A presence of eosinophils and a reduced density of the cardiac striated muscle fibers were also visible in the Dox-treated hearts under enhanced magnification (Fig. 5B). This implies that targeted and untargeted hyperbranched polymeric nanomedicines provide a safer alternative for direct chemotherapy, while also leading to enhanced accumulation of the drug in tumour tissue. Together, this study shows that brain cancers with multiple tumour suppressor mutations can be slowed when treated with a HBP loaded with Dox if the treatment is started at an early gadolinium-permeable stage, with reduced commensurate unwanted side-effects.

3.7. HBPs as brain chemotherapy carriers

Similar HBPs loaded with Dox have been used extensively in our group, for example to target solid tumours including breast cancer and prostate cancer with promising success [7,8]. As Dox has been extensively used to study delivery and diffusion, here it is used as a model therapeutic to further understand the distribution of chemotherapies delivered by nanomedicines in brain tumours. The dose of Dox used was chosen based on toxicology studies, and our most recent study to treat breast cancer in a xenograft model [7]. While previous studies investigating brain tumour and glioblastoma treatments using orthotopic xenograft models found a stronger effect of slowing tumour growth than that which is observed here [35], the brain cancer model used in this study appeared to be more aggressive based on the rapid growth in the vehicle control group. It is important to also note that although there was gadolinium permeability during treatment, in some cases areas of the tumour appeared to maintain higher BBB integrity, leading to a relatively more rapid and therefore heterogeneous expansion in these tumour areas despite treatment. This signifies one of the key challenges in developing and understanding new strategies for treating brain tumours. Ultimately, the HBP and BsAb + HBP groups showed more promising long-term protective effects, including after treatment had finished, compared to the Dox group, and this could be explained to some extent by the EPR effect maintaining a steady dose of the longer circulating HBP in the leaky tumour area. Free Dox has a short initial half-life of only 5 min due to its rapid excretion via bile, followed by a steady half-life of 17 h in the blood [36]. It also has poor lipophilicity, and is effluxed by P-glycoprotein transporters in the BBB [37]. In congruence with these factors suggesting Dox to be a sub-optimal therapy for brain cancer, we found HBP affected a more widespread volume within the tumour compared to Dox alone, and this is probably one of the reasons for its enhanced efficacy. It is also evident that HBP-loaded Dox is a safer method of delivery than Dox alone, as there was no bodyweight loss or cardiomyopathy in the HBP treated mice. Left ventricular cardiomyopathy induced by doxorubicin has been previously reported in literature, including in larger animal models [38], and we have also previously found that dox-loaded nanomedicines do not change bodyweight over prolonged treatment regimes, whereas free Dox does [21].

This is one of the first studies to our knowledge that has shown reduced growth of brain tumours in a novel highly aggressive genetic glioblastoma model using nanomedicines and BsAbs to target the cancer cells. These results follow on from recent work in our lab, which identified that the brain cancer progression is significantly accelerated by BBB leakiness [13]. We then used this property as a criterion to initiate treatment as determined by the diagnostic capabilities of MRI. Previous studies have investigated the use of a Dox-loaded poly-sorbate coated nanoparticle to treat stereotaxically injected cancer cells in a rat model [39,40], with similarly successful treatment. The reasoning behind using poly-sorbate to coat the polymer is that this binds to plasma proteins, and therefore can more easily cross the BBB through receptor-mediated transcytosis. While these studies induced tumour growth in the same area of the brain each time with a single cell line, we set out to assess the case-by-case efficacy and distribution of our therapeutic in genetically induced glioma model with variable sites of tumour initiation in each animal. Therefore, non-tumoural brain integrity at disease onset and immune response were maintained in this mouse model, as there was no invasive stereotaxic injection surgery or immunodeficiency. Any nanomedicine that crossed into the brain occurred as a function of impaired localised integrity of the BBB as a function of tumour growth, and it appeared that the tumour inevitably spread into BBB-intact areas in this model, despite promising reductions in growth during the treatment period. We believe this is a key parameter for understanding how these materials cross into the brain and ultimately provide an efficacious effect.

4. Conclusions

This study adds a proof-of-concept to the growing literature showing the improved safety and effectiveness of chemotherapeutics delivered by nanomedicines and future translation of cancer-targeted hyperbranched polymers. Moreover, this study is the first BsAb targeted HBP for treatment of GBM using a spontaneous model, and also the first time treatment has been monitored in real-time using ultra high-field MRI. Despite the variability in the genetic model leading to significant differences in tumours that were formed and this subsequently meaning we couldnot feasibly do a full survival and therapeutic assessment, we have shown here that brain tumour growth can be prevented in a targeted case-by-case manner using stealth HBPs and BsAbs to release chemotherapy payloads into areas of glioma leakiness. When HBP-Dox is delivered at an early leaky stage of brain cancer, it could effectively slow disease progression by over 90%, and as confirmed in previous reports, these nanomedicines can also be targeted efficiently using cancer marker-specific BsAbs. This is further benefited by a demonstrated improved safety profile, adding to a growing literature of the improved safety of nanoparticles for treating brain cancer [34], and a projected 2–7x improvement in survival time while maintaining quality of life. Despite these improvements, the growth of GBM into BBB-intact areas remains a challenge to be solved. Overall, the data presented in this manuscript suggest HBPs have the potential to be used concurrently with standard treatment options, including surgery and novel radiotherapy techniques such as dose painted gamma radiosurgery (e.g. Gamma Knife®) [41]. This combinatorial approach could improve patient quality of life by continuously targeting new areas of leaky angiogenesis whilst also reducing peripheral organ off-target effects of the chemotherapy.

Author statement

Phillip W. Janowicz: Methodology, Data curation, Writing – original draft; **Zachary H. Houston**: Conceptualisation, Methodology, reviewing and editing; **Jens Bunt**: Methodology, Funding acquisition; **Nicholas L. Fletcher**: Methodology, Conceptualisation; **Craig A. Bell**: Methodology, reviewing and editing; **Gary Cowin**: Methodology; **Christopher B. Howard**: Methodology; **Dewan Taslima**: Methodology; **Nicholas Westra van Holthe**: Methodology, Data curation; **Amber Prior**: Methodology, Data curation; **Vanessa Soh**: Methodology, Data curation; **Saikat Ghosh**: Methodology, Data curation; **James Humphries**: Methodology; **Pie Huda**: Data curation, Methodology; **Stephen M. Mahler**: Methodology; **Linda J. Richards**: Methodology, Funding acquisition; **Kristofer J. Thurecht**: Methodology, Supervision, Project administration, Funding acquisition, Conceptualisation, Writing – review & editing

Author's contributions

P·W.J, **Z.H·H**, **N.L.F**, and **K.J.T**. designed the study. **P.W.J**. manufactured the HBP and performed the experiments. **J.B.** and **L.J.R**. provided guidance for the mouse model and biological resources. **C.A.B**.

and **D.T**. provided guidance for the manufacturing of the HBP. **C.B.H**, **P. H.** and **S.M.M**. manufactured and provided the BsAb. **N.W.V.H**. provided guidance for the MSOT. **A.P**. and **V.S**. helped perform HPLC operation and analysis. SDS-PAGE was completed with help from **S.G**. **J. H**. provided help with GPC-MALLS. **P.W.J**. wrote the manuscript and all authors contributed to the interpretation of data and editing of the manuscript. **K.J.T**. approved the final version of the manuscript.

Funding

P·W.J. was supported by an Australian Postgraduate Award funded by the Australian Government. We acknowledge the National Health and Medical Research Council for fellowship support (K.J.T.; APP1148582). Animal development and breeding funding was provided by Tour de Cure (Young Research Grant to J.B.); Brain Foundation (research gift to J.B.); Ride for Rhonda (research gift to L.J.R. and J.B.) and private donations to the Queensland Brain Institute for brain cancer research. L.J.R. is supported by a NHMRC Principal Research Fellowship (GNT1120615). Research was funded through the ARC Centre of Excellence in Convergent BioNano Science and Technology (CE140100036) and in part by the ARC Training Centre for Innovation in Biomedical Imaging Technologies (IC170100035).

Data availability

All data is presented in the paper and supplementary information, and available from the corresponding author upon request.

Declaration of competing interest

The authors declare that they have no known competing financial interests or personal relationships that could have appeared to influence the work reported in this paper.

Acknowledgements

The authors acknowledge the facilities, and the scientific and technical assistance of the National Imaging Facility at the Centre for Advanced Imaging, University of Queensland. All microscopy was completed in the Queensland Brain Institute (QBI) Advanced Microscopy Facility. We are also grateful for histological advice from Robert Sullivan at the QBI Histology Facility. NMR Spectroscopy was performed at the Centre for Advanced Imaging NMR Facility with training and help from Gregory Pierens. HPLC was performed at the Centre for Microscopy and Microanalysis (CMM), with training and help from Brett Hamilton. GPC-MALLS and FTIR instruments were provided by the Australian National Fabrication Facility (ANFF), with training and help from Javaid Khan. Mice were cared for and monitored by UQ Biological Resources. Training for tail vein injections was provided by Kim Woolley at QBI.

Appendix A. Supplementary data

Supplementary data to this article can be found online at https://doi.org/10.1016/j.biomaterials.2022.121416.

References

[1] M. Koshy, J.L. Villano, T.A. Dolecek, A. Howard, U. Mahmood, S.J. Chmura, R. R. Weichselbaum, B.J. McCarthy, Improved survival time trends for glioblastoma using the SEER 17 population-based registries, J. Neuro Oncol. 107 (1) (2012) 207–212, https://doi.org/10.1007/s11060-011-0738-7.

[2] Australian Institute of Health and Welfare, Cancer Data in Australia, 2020. Available from: https://www.canceraustralia.gov.au/affected-cancer/cancer-types/brain-cancer/statistics. (Accessed 16 September 2020).

[3] A.P. Patel, J.L. Fisher, E. Nichols, F. Abd-Allah, J. Abdela, A. Abdelalim, H. N. Abraha, D. Agius, F. Alahdab, C. Fitzmaurice, GBD 2016 brain and other CNS cancer collaborators, global, regional, and national burden of brain and other CNS cancer, 1990–2016: a systematic analysis for the global burden of disease study 2016, Lancet Neurol. 18 (4) (2019) 376–393, https://doi.org/10.1016/S1474-4422(18)30468-X.

[4] M.E. Davis, Glioblastoma: overview of disease and treatment, Clin. J. Oncol. Nurs. 20 (5) (2016) S2, https://doi.org/10.1188/16.CJON.S1.2-8.

[5] J. Humphries, D. Pizzi, S.E. Sonderegger, N.L. Fletcher, Z.H. Houston, C.A. Bell, K. Kempe, K.J.J.B. Thurecht, Hyperbranched poly(2-oxazoline)s and poly(ethylene glycol): a structure–activity comparison of biodistribution, Biomacromolecules 21 (8) (2020) 3318–3331, https://doi.org/10.1021/acs.biomac.0c00765.

[6] L. Chen, J.D. Simpson, A.V. Fuchs, B.E. Rolfe, K.J.J.M.p. Thurecht, Effects of surface charge of hyperbranched polymers on cytotoxicity, dynamic cellular uptake and localization, hemotoxicity, and pharmacokinetics in mice, Mol. Pharm. 14 (12) (2017) 4485–4497, https://doi.org/10.1021/acs.molpharmaceut.7b00611.

[7] Y. Zhao, N.L. Fletcher, T. Liu, A.C. Gemmell, Z.H. Houston, I. Blakey, K.J. Thurecht, In vivo therapeutic evaluation of polymeric nanomedicines: effect of different targeting peptides on therapeutic efficacy against breast cancer, Nanotheranostics 2 (4) (2018) 360, https://doi.org/10.7150/ntno.27142.

[8] A.K. Pearce, A.V. Fuchs, N.L. Fletcher, K.J. Thurecht, Targeting nanomedicines to prostate cancer: evaluation of specificity of ligands to two different receptors in vivo, Pharm. Res. (N. Y.) 33 (10) (2016) 2388–2399, https://doi.org/10.1007/s11095-016-1945-x.

[9] J. Wykosky, D.M. Gibo, C. Stanton, W.J. Debinski, EphA2 as a novel molecular marker and target in glioblastoma multiforme, Mol. Cancer Res. 3 (10) (2005) 541–551, https://doi.org/10.1158/1541-7786.MCR-05-0056.

[10] F. Ciardiello, G.J. Tortora, Epidermal growth factor receptor (EGFR) as a target in cancer therapy: understanding the role of receptor expression and other molecular determinants that could influence the response to anti-EGFR drugs, Eur. J. Cancer 39 (10) (2003) 1348–1354, https://doi.org/10.1016/s0959-8049(03)00235-1.

[11] A.L. Vescovi, E. Binda, T. Mazza, F. Dimeco, EphrinA2 Receptor in human gliolbastoma cancer stem cells and identification of new putative therapeutic targets, Neuro Oncol. 16 (Suppl 3) (2014) iii34, https://doi.org/10.1093/neuonc/nou208.42.

[12] C.B. Howard, N. Fletcher, Z.H. Houston, A.V. Fuchs, N.R. Boase, J.D. Simpson, L. J. Raftery, T. Ruder, M.L. Jones, C.J. de Bakker, Overcoming instability of antibody-nanomaterial conjugates: next generation targeted nanomedicines using bispecific antibodies, Adv. Health. Mat. 5 (16) (2016) 2055–2068, https://doi.org/10.1002/adhm.201600263.

[13] Z.H. Houston, J. Bunt, K.-S. Chen, S. Puttick, C.B. Howard, N.L. Fletcher, A. V. Fuchs, J. Cui, Y. Ju, G. Cowin, Understanding the uptake of nanomedicines at different stages of brain cancer using a modular nanocarrier platform and precision bispecific antibodies, ACS Cent. Sci. 6 (5) (2020) 727–738, https://doi.org/10.1021/acscentsci.9b01299.

[14] C.F. Thorn, C. Oshiro, S. Marsh, T. Hernandez-Boussard, H. McLeod, T.E. Klein, R. B. Altman, Doxorubicin pathways: pharmacodynamics and adverse effects, Pharmacogenetics Genom. 21 (7) (2011) 440, https://doi.org/10.1097/FPC.0b013e32833ffb56.

[15] M.S. Lesniak, U. Upadhyay, R. Goodwin, B. Tyler, H. Brem, Local delivery of doxorubicin for the treatment of malignant brain tumors in rats, Anticancer Res. 25 (6B) (2005) 3825–3831. Available from: https://www.ncbi.nlm.nih.gov/pmc/articles/PMC1635000/. (Accessed 16 September 2020).

[16] E. Graham-Gurysh, K.M. Moore, A.B. Satterlee, K.T. Sheets, F.-C. Lin, E. M. Bachelder, C.R. Miller, S.D. Hingtgen, K.M. Ainslie, Sustained delivery of doxorubicin via acetalated dextran scaffold prevents glioblastoma recurrence after surgical resection, Mol. Pharm. 15 (3) (2018) 1309–1318, https://doi.org/10.1021/acs.molpharmaceut.7b01114.

[17] V. Matcovschii, D. Lisii, V. Gudumac, S. Dorosenco, Selective interstitial doxorubicin for recurrent glioblastoma, Clin Case Rep 7 (12) (2019) 2520–2525, https://doi.org/10.1021/acs.molpharmaceut.7b01114.

[18] K.B. Wallace, Doxorubicin-induced cardiac mitochondrionopathy, J. Pharmacol. Toxicol. 93 (3) (2003) 105–115, https://doi.org/10.1034/j.1600-0773.2003.930301.x.

[19] Y. Bae, S. Fukushima, A. Harada, K. Kataoka, Design of environment-sensitive supramolecular assemblies for intracellular drug delivery: polymeric micelles that are responsive to intracellular pH change, Angew. Chem. 115 (38) (2003) 4788–4791, https://doi.org/10.1002/anie.200250653.

[20] M. Hrubý, Č. Koňák, K. Ulbrich, Polymeric micellar pH-sensitive drug delivery system for doxorubicin, J. Con. Rel. 103 (1) (2005) 137–148, https://doi.org/10.1016/j.jconrel.2004.11.017.

[21] A.K. Pearce, J.D. Simpson, N.L. Fletcher, Z.H. Houston, A.V. Fuchs, P.J. Russell, A. K. Whittaker, K.J.J.B. Thurecht, Localised delivery of doxorubicin to prostate cancer cells through a PSMA-targeted hyperbranched polymer theranostic, Biomaterials 141 (2017) 330–339, https://doi.org/10.1016/j.biomaterials.2017.07.004.

[22] C. Zhao, H. Wang, C. Xiong, Y.J.B. Liu, b.r. communications, Hypoxic glioblastoma release exosomal VEGF-A induce the permeability of blood-brain barrier, Biochem. Biophys. Res. Commun. 502 (3) (2018) 324–331, https://doi.org/10.1016/j.bbrc.2018.05.140.

[23] K. Schoenegger, S. Oberndorfer, B. Wuschitz, W. Struhal, J. Hainfellner, D. Prayer, H. Heinzl, H. Lahrmann, C. Marosi Grisold, Peritumoral edema on MRI at initial diagnosis: an independent prognostic factor for glioblastoma? Eur. J. Neurol. 16 (7) (2009) 874–878, https://doi.org/10.1111/j.1468-1331.2009.02613.x.

[24] The Cancer Geneome Atlas Research Network (CGARN), Comprehensive genomic characterization defines human glioblastoma genes and core pathways, Nature 455 (7216) (2008) 1061, https://doi.org/10.1038/nature07385.

[25] C.J. Belden, P.A. Valdes, C. Ran, D.A. Pastel, B.T. Harris, C.E. Fadul, M.A. Israel, K. Paulsen, D.W.J.R. Roberts, Genetics of glioblastoma: a window into its imaging

and histopathologic variability, Radiographics 31 (6) (2011) 1717–1740, https://doi.org/10.1148/rg.316115512.
[26] L.M. Chow, R. Endersby, X. Zhu, S. Rankin, C. Qu, J. Zhang, A. Broniscer, D. W. Ellison, S. Baker, Cooperativity within and among Pten, p53, and Rb pathways induces high-grade astrocytoma in adult brain, Cancer Cell 9 (3) (2011) 305–316, https://doi.org/10.1016/j.ccr.2011.01.039, 18.
[27] L.M. Chow, S. Baker, Capturing the molecular and biological diversity of high-grade astrocytoma in genetically engineered mouse models, Oncotarget 3 (1) (2012) 67, https://doi.org/10.18632/oncotarget.425.
[28] E.A. Eisenhauer, P. Therasse, J. Bogaerts, L.H. Schwartz, D. Sargent, R. Ford, J. Dancey, S. Arbuck, S. Gwyther, M.J. Mooney, New response evaluation criteria in solid tumours: revised RECIST guideline (version 1.1), Eur. J. Cancer 45 (2) (2009) 228–247.
[29] A.V. Fuchs, B.W. Tse, A.K. Pearce, M.-C. Yeh, N.L. Fletcher, S.S. Huang, W. D. Heston, A.K. Whittaker, P.J. Russell, K.J. Thurecht, Evaluation of polymeric nanomedicines targeted to PSMA: effect of ligand on targeting efficiency, Biomacromolecules 16 (10) (2015) 3235–3247, https://doi.org/10.1021/acs.biomac.5b00913.
[30] M. Faria, M. Björnmalm, K.J. Thurecht, S.J. Kent, R.G. Parton, M. Kavallaris, A. P. Johnston, J.J. Gooding, S.R. Corrie, B.J.J.N.n. Boyd, Minimum information reporting in bio–nano experimental literature, Nat. Nanotechnol. 13 (9) (2018) 777–785, https://doi.org/10.1038/s41565-018-0246-4.
[31] A.K. Pearce, B.E. Rolfe, P.J. Russell, B.W.-C. Tse, A.K. Whittaker, A.V. Fuchs, K. J. Thurecht, Development of a polymer theranostic for prostate cancer, Polym. Chem. 5 (24) (2014) 6932–6942, https://doi.org/10.1039/C4PY00999A.
[32] N. Fletcher, Z. Houston, J. Simpson, R. Veedu, K.J. Thurecht, Designed multifunctional polymeric nanomedicines: long-term biodistribution and tumour accumulation of aptamer-targeted nanomaterials, Chem. Commun. 54 (82) (2018) 11538–11541, https://doi.org/10.1039/C8CC05831H.
[33] Y. Zhao, Z.H. Houston, J.D. Simpson, L. Chen, N.L. Fletcher, A.V. Fuchs, I. Blakey, K.J.J.M.p. Thurecht, Using peptide aptamer targeted polymers as a model nanomedicine for investigating drug distribution in cancer nanotheranostics, Mol. Pharm. 14 (10) (2017) 3539–3549, https://doi.org/10.1021/acs.molpharmaceut.7b00560.
[34] M. Björnmalm, K.J. Thurecht, M. Michael, A.M. Scott, F. Caruso, Bridging bio–nano science and cancer nanomedicine, ACS Nano 11 (10) (2017) 9594–9613, https://doi.org/10.1021/acsnano.7b04855.
[35] L.P. Ganipineni, F. Danhier, V. Préat, Drug delivery challenges and future of chemotherapeutic nanomedicine for glioblastoma treatment, J. Con. Rel. 281 (2018) 42–57, https://doi.org/10.1016/j.jconrel.2018.05.008.
[36] A. Rahman, D. Carmichael, M. Harris, J.K. Roh, Comparative pharmacokinetics of free doxorubicin and doxorubicin entrapped in cardiolipin liposomes, Cancer Res. 46 (5) (1986) 2295–2299. Available from: https://cancerres.aacrjournals.org/content/canres/46/5/2295.full.pdf. (Accessed 16 September 2020).
[37] E.D. Hugger, K.L. Audus, R. Borchardt, Effects of poly (ethylene glycol) on efflux transporter activity in Caco-2 cell monolayers, J. Pharm. Sci. 91 (9) (2002) 1980–1990, https://doi.org/10.1002/jps.10175.
[38] S. Christiansen, A. Perez-Bouza, G. Schälte, R.-D. Hilgers, R. Autschbach, Selective left ventricular adriamycin-induced cardiomyopathy in the pig, J. Heart Lung Transplant. 27 (1) (2008) 86–92, https://doi.org/10.1016/j.healun.2007.10.003.
[39] S.C. Steiniger, J. Kreuter, A.S. Khalansky, I.N. Skidan, A.I. Bobruskin, Z. S. Smirnova, S.E. Severin, R. Uhl, M. Kock, K.D. Geiger, Chemotherapy of glioblastoma in rats using doxorubicin-loaded nanoparticles, Int. J. Cancer 109 (5) (2004) 759–767, https://doi.org/10.1002/ijc.20048.
[40] S. Wohlfart, A.S. Khalansky, S. Gelperina, O. Maksimenko, C. Bernreuther, M. Glatzel, J. Kreuter, Efficient chemotherapy of rat glioblastoma using doxorubicin-loaded PLGA nanoparticles with different stabilizers, PLoS One 6 (5) (2011), https://doi.org/10.1371/journal.pone.0019121.
[41] B.S. Imber, I. Kanungo, S. Braunstein, I.J. Barani, S.E. Fogh, J.L. Nakamura, M. S. Berger, E.F. Chang, A.M. Molinaro, J. Cabrera, Indications and efficacy of gamma knife stereotactic radiosurgery for recurrent glioblastoma: 2 decades of institutional experience, Neurosurgery 80 (1) (2017) 129–139, https://doi.org/10.1227/NEU.0000000000001344.